IEEE Access
Multidisciplinary ⋮ Rapid Review ⋮ Open Access Journal

Received April 20, 2022, accepted May 25, 2022, date of publication May 30, 2022, date of current version June 9, 2022.

Digital Object Identifier 10.1109/ACCESS.2022.3178952

Hybrid Force/Velocity Control for Simulating Contact Dynamics of Satellite Robots on a Hardware-in-the-Loop Simulator

JUN HE AND MINGJIN SHEN

State Key Laboratory of Mechanical System and Vibration, School of Mechanical Engineering, Shanghai Jiao Tong University, Shanghai 200240, China

Corresponding author: Jun He (jhe@sjtu.edu.cn)

This work was supported in part by the National Natural Science Foundation of China under Grant 52175022, in part by the State Key Laboratory of Mechanical System and Vibration under Grant MSVZD202106, and in part by the Shanghai Research and Development Public Service Platform Project under Grant 19DZ2291400.

ABSTRACT Contact operations of free-floating satellite robots are difficult and risky and therefore, they must be thoroughly tested and verified by ground-based facilities. A hardware-in-the-loop (HIL) simulation system with industrial robots is commonly used for simulating space robotic operations. However, a great challenge is to handle simulation divergence due to intrinsic time delay between the measured forces and the simulation driven reaction of the robot. This paper presents a novel hybrid force/velocity control method for compensating the time delay of a HIL simulation. A real-time identification method for contact stiffness and damping is proposed based on the adaptive Kalman filter. Then, an energy observer is designed to monitor the energy flow and an energy controller (EC) is established. The EC acts a variable damping and thus the contact damping is amended. Therefore, a compensation strategy based on parameter identification and damping amendment is proposed to eliminate the effects of time delays. Finally, numerical simulations and experimental results show that the simulation divergence due to time delay can be prevented. Moreover, space robotic operations with high fidelity of both contact force and contact velocity are reproduced by the proposed method.

INDEX TERMS Hardware-in-the-loop (HIL) simulation, contact stiffness, contact damping, identification, space robotic operation.

I. INTRODUCTION

Space robotic operations have become more common than ever with the increase of space activities such as satellite on-orbit servicing and deorbiting space debris [1], [2]. Robotic operations in space are very difficult and risky and therefore, ground experiments must be conducted to verify the reliability of the design and control method of a space robotic system [3]. The hardware-in-the-loop (HIL) simulation, which is also referred to hybrid simulation, can provide zero-gravity (0-g) virtual environment in real time and thus it is often used to perform the on-ground verification tests [4]. For a HIL simulation, both hardware and numerical software are incorporated in the simulation loop. The hardware components (such as docking mechanisms) collide with each other to produce the contact force and moment. The contact force and moment are measured by a six-axis force/torque (F/T) sensor and taken as the inputs of a numerical software with respect to satellite dynamics to calculate motion trajectories of two satellites. Then, the robotic simulator tracks the trajectories and reproduces the motion of two satellites [5].

The main problem with HIL simulation is a simulation divergence resulting from the time delay, which occurs mainly between the measured forces and the simulation driven reaction of the robot [6]. The time delay causes an energy increase, which means the work done by the rebounding force is greater than the work done by the resistance force [7]. Thus, the rebound velocity is larger than the approach velocity for each collision. This divergence distortion in the simulation renders the simulation system unstable. Accordingly, the tested hardware is very likely to be damaged owing to large impact force, and the simulation experiment cannot be continued.

The associate editor coordinating the review of this manuscript and approving it for publication was Shun-Feng Su.

The direct compensation method for the delay is to modify contact forces in real time during the HIL simulation. It requires real-time identification of contact parameters, including stiffness and damping [8]. Contact parameter estimation is critical for force tracking and impedance control during the constrained motion of a robotic system. For example, the identification of contact parameters can be employed to establish an accurate model of contact force, which is essential to ensure the success of capturing a non-cooperative target [9]. Yu *et al.* [10], [11] proposed a force and displacement compensation method based on three degree-of-freedom (3-DOF) stiffness and damping real-time identification. There are some typical approaches to contact parameter estimation: the signal processing method [12], indirect adaptive controller [13], model reference adaptive controller (MRAC) [14], recursive least squares (RLS) estimation [15], and adaptive Kalman filter [16]. Although parameter identification is an appealing approach for exact force compensation, there still exist some challenges hindering its application to robotic simulators with large time delay. So far, it has only been applied to a few parallel robotic facilities with relatively high stiffness. For example, the time delay of the parallel robotic simulator in [7]–[8] is less than 10 ms. However, serial simulators using industrial robots have lower stiffness and weaker dynamic response capability, which leads to dozens of time delays [17].

Control algorithms based on the principle of energy conservation are alternative solutions for time delay compensation. For example, the passivity-based control (PBC) is a typical algorithm [18]. The PBC has been used to handle unstable systems caused by time delay [19], such as haptics and teleoperation systems [20], [21]. Hannaford and Spong [22] and Ryu *et al.* [23] proposed a passivity observer and a passivity controller to handle the time delay of haptic interface, which is also called the time-domain passivity approach (TDPA) [24]. Recently, Stefano *et al.* [25] exploited this method for rendering the free-floating dynamics of a satellite with a robot on an HIL simulator. The TDPA method can deal with a time delay of up to 40 ms [18], [25]. However, the TDPA adjusts contact velocities to conform to energy conservation and thus the accuracy of contact force is inevitably sacrificed. Thus, large contact forces are likely to occur, which will damage tested instruments. In addition, these methods cannot consider the work done by the damping force, which should be converted into heat energy and then dissipate for the HIL simulation to obtain velocity characteristics close to real physical contact. To accomplish this, the contact damping must be identified online.

The main contribution of this study is to propose a hybrid force/velocity control method for compensating the time delay in a HIL simulation. This method utilizes the contact parameter identification and the damping amendment to calculate the compensation force. The entire control scheme includes a satellite dynamics module, a compensation module, an energy observer and an energy controller. The approach can prevent the simulation divergence due to the time delay and reproduce the real contact process during space robotic operations. It achieves high fidelity for both contact force and contact velocity. Finally, the proposed control strategy is validated by both numerical simulations and practical HIL simulation experiments.

The remainder of this study is organized as follows. The HIL simulation system is described in Section 2. The compensation method based on parameter identification and damping amendment is proposed in Section 3. Sections 4 and 5 present simulations and experiments, respectively. Finally, the conclusions of the study are given in Section 6.

II. DESCRIPTION OF THE HIL SIMULATION SYSTEM

A. EXPERIMENTAL SETUP

Figure 1 shows the HIL simulation system. It consists of a motion simulator of a service satellite, a mockup of a target satellite, a space robot, and a docking imitation mechanism. The motion simulator is a 6-DOF industrial robot (*EFFORT*, ER210-2700) mounted on a 12-meter long rail system. Since only the relative motion between the two satellites is of interest, one simulator is enough to simulate the relative motion between the satellites. Here, the simulator for the target satellite is replaced by a stationary satellite mock-up with one part of a docking imitation mechanism. The mockup of the target satellite includes the typical geometrical characteristics of the satellite. During experiments, the robotic simulator delivers relative motion between servicing and target satellites because the mockup of the target satellite is stationary. The space robot is a 6-DOF serial robot. The docking imitation mechanism consists of a steel cylinder rod and a collision frame. The collision rod is installed at the end of the space robot. The collision frame is connected to the mockup of the target satellite by a six-axis F/T sensor (*Sunrise*, M4344D). This sensor is adopted to measure the contact force between the rod and the frame.

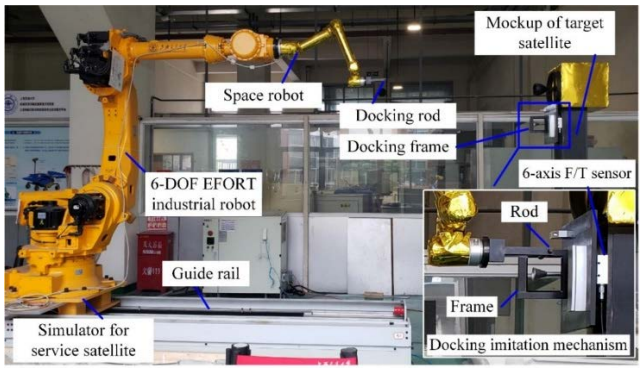

FIGURE 1. Prototype of the HIL simulator.

To illustrate the relationship between the real contact dynamics in space and the dynamics rendered in the robotic facility, two groups of coordinate systems are established, one for the HIL simulation system and one for the satellite system, as shown in Fig. 2. There are four assembly frames:

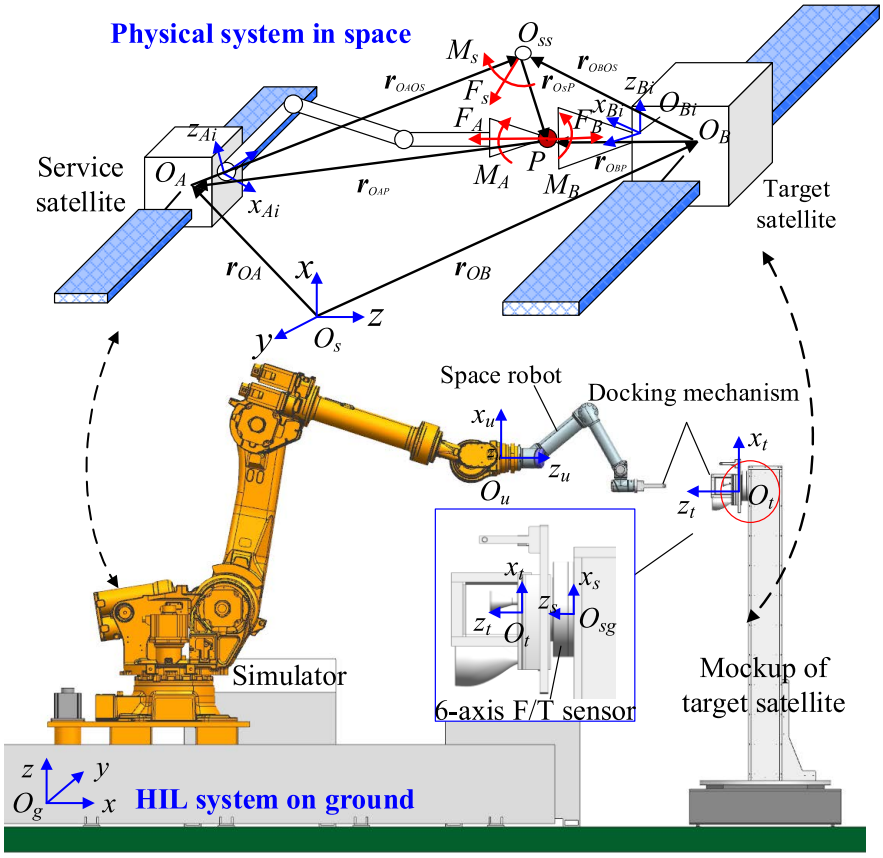

FIGURE 2. Coordinate systems of the HIL simulation system.

O_{Ai}-xyz and O_{Bi}-xyz on the service and target satellites, and O_{u}-xyz and O_{t}-xyz on the service satellite simulator and the mockup of the target satellite. The relative position between O_{u}-xyz and O_{t}-xyz is the same as the relative position between O_{Ai}-xyz and O_{Bi}-xyz, that is, ${}^{O_u}\mathbf{T}_{O_t} = {}^{O_{Ai}}\mathbf{T}_{O_{Bi}}$. There are two sensor frames: O_{sg}-xyz on the mockup of the target satellite, and O_{ss}-xyz on the target satellite. The transformation matrix from Frame O_{ss}-xyz to Frame O_{Bi}-xyz in space is the same as the transformation matrix between Frame O_{t}-xyz and Frame O_{sg}-xyz on the ground. In addition, two mass center frames, O_{A}-xyz and O_{B}-xyz, are located on the service and target satellites, respectively.

B. TIME DELAY EFFECTS

In the HIL simulation, satellite dynamic behaviors are calculated by a mathematical model of satellite dynamics, and the full six-degrees-of-freedom (6-DOF) collision process is produced by real docking mechanisms. The contact force is measured by the F/T sensor. Then, to obtain the motion trajectories of the two satellites, the measured contact forces are the inputs of the desired dynamic model a free-floating satellite, which is given by

$$\dot{\boldsymbol{v}}_c = M^{-1}{}_s^c\mathbf{R}\mathbf{F}_s, \tag{1}$$

$$\dot{\boldsymbol{\omega}}_c = \boldsymbol{I}^{-1}[\boldsymbol{I}\boldsymbol{\omega}_c \times \boldsymbol{\omega}_c + \boldsymbol{r}_{c,s} \times ({}_s^c\boldsymbol{R}\boldsymbol{F}_s) + {}_s^c\boldsymbol{R}\boldsymbol{\tau}_{\mathrm{s}}], \tag{2}$$

where $\boldsymbol{F}_{\mathrm{s}}$ and τ_{s} are the force and moment measured by the six-axis F/T sensor, respectively; $\boldsymbol{v}_{\mathrm{c}}$and ω_{c} are the linear velocity of the center of mass (CoM) of the satellite and the angular velocity of the satellite; $\boldsymbol{M}$ is the mass matrix of the satellite; $\boldsymbol{I}$ is the inertia matrix of the satellite with respect to the coordinate system at the CoM; ${}_s^c\boldsymbol{R}$ is the rotation matrix from the sensor frame to the CoM frame; $\boldsymbol{r}_{\mathrm{c,s}}$ is the vector from the origin of the sensor frame to the origin of the CoM frame. For practical space operations, motions of a space robot affect the solutions of Eq. (1) and (2). However, considering that the main issue of this work is to deal with the time delay, motions of the space robot are not involved in this study. The space robot retains a fixed configuration during the following simulations and experiments.

Ideally, the robotic simulator strictly tracks the motion trajectories of the satellites. The joint inputs of the simulator can be calculated according to the inverse kinematics. Therefore, the dynamic behaviors of two satellites in space can be reproduced by a HIL simulation on the ground. However, there exists time delay between the measured forces and the simulation driven reaction of the robot. The time delay comes from two aspects, as seen in Fig.3. One aspect is the sensor system including the force sensor, amplifier, data acquisition card, and signal filter. For the sensor system, there is a time delay with an identifiable and fixed value, which is

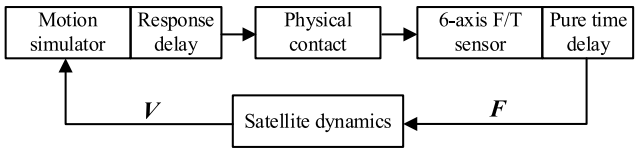

FIGURE 3. Schematic of time delay effect.

called pure time delay. The other is a dynamic response delay of the robotic simulator, which is unknown and difficult to be modelled. As aforementioned, the time delay leads to a simulation divergence, which must be prevented.

III. COMPENSATION METHODOLOGY

A. STIFFNESS AND DAMPING IDENTIFICATION

Compared with satellites, docking mechanisms and robotic operation tools are significantly smaller. The physical contact occurring in robotic operations can be regarded as a point contact. At time t, the practical displacement and velocity of the contact point can be calculated using the forward kinematic model of the robotic simulator, as seen in Fig. 4(a), which are given by

$$\boldsymbol{p}_{Op}(t) = \boldsymbol{p}_{act}(t) + \boldsymbol{R}_{act}(t)\boldsymbol{r}_{Op}^{Oe}(t), \tag{3}$$

$$\boldsymbol{v}_{Op}(t) = \boldsymbol{v}_{act}(t) + \omega_{act}(t) \times \{\boldsymbol{R}_{act}(t)\boldsymbol{r}_{Op}^{Oe}(t)\}. \tag{4}$$

where P(t) represents the contact point positions. *Surf*(0) and *Surf*(t) in Fig. 4(b) denote the initial contact surface and the contact surface at time t, respectively.

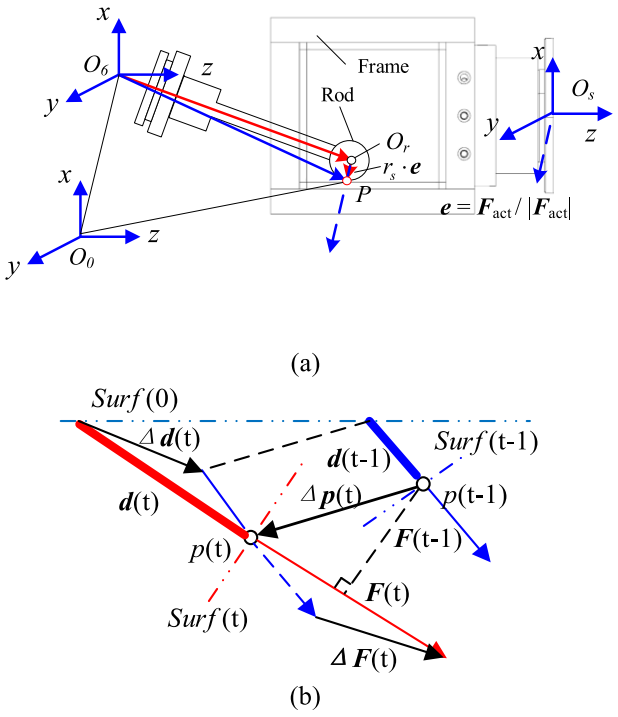

FIGURE 4. Schematic of contact analysis. (a) Position of contact point. (b) Contact force and deformation.

At time t, the relationship between the contact force and the penetration is described by a mass-spring-damper system without friction, which is denoted by

$$\boldsymbol{F}(t) = k_d \cdot d(t) + c_d \cdot \dot{d}(t), \tag{5}$$

where d(t) is the penetration; and $\boldsymbol{F}$(t) is the contact force. Note that the penetration d(t) is unknown. To identify the contact stiffness and damping, two assumptions are made.

The first assumption is that the contact between docking mechanisms is a point contact, which only leads to the force. The moment measured by the six-axis F/T sensor is produced by the contact force. Thus, the increment of contact deformation $\Delta\boldsymbol{d}$(t) should be in alignment with the increment of the contact force $\Delta\boldsymbol{F}$(t), as seen in Fig. 4(b). Note that there is a pure time delay from the actual force $\boldsymbol{F}_{\text{act}}$ to the measured force $\boldsymbol{F}_{\text{mea}}$. The pure time delay τ_{p} is compensated by a low-pass filter, which is given by

$$\boldsymbol{F}_{mea}(t) = \boldsymbol{L}^{-1}[\boldsymbol{G}(s)]\boldsymbol{F}_{act}(t), \tag{6}$$

where $\boldsymbol{G}(s) = 1 + \tau_p s$ is the transfer function; $\boldsymbol{L}^{-1}[\boldsymbol{G}(s)]$ is the inverse Laplace transformation; and $\boldsymbol{F}_{\boldsymbol{act}}$(t) is the compensated contact force for the measurement delay. Furthermore, the direction vector of the practical contact force in Fig. 4(a) is described by

$$\boldsymbol{e} = \frac{\boldsymbol{F}_{act}(t)}{|\boldsymbol{F}_{act}(t)|}. \tag{7}$$

The second assumption is that since the sampling time is very short, the contact stiffness and damping do not change. The projection of the displacement and velocity vector at the contact point in the direction of the contact force is calculated. Then, the projection increments of displacement and velocity are used for estimating the contact parameters, which are written as

$$\Delta p_{act} = \{\boldsymbol{p}_{Op}(t) - \boldsymbol{p}_{Op}(t-1)\} \cdot \boldsymbol{e}, \tag{8}$$

$$\Delta v_{act} = \{\boldsymbol{v}_{Op}(t) - \boldsymbol{v}_{Op}(t-1)\} \cdot \boldsymbol{e}, \tag{9}$$

$$\Delta F_{act} = \boldsymbol{F}_{act}(t) - \boldsymbol{F}_{act}(t-1), \tag{10}$$

where $\boldsymbol{p}_{\text{Op}}$ and $\boldsymbol{v}_{\text{Op}}$ are the practical position and velocity, respectively.

The adaptive Kalman filter (AKF) is adopted for the estimation of the contact stiffness and damping. The conventional Kalman filter of a linear dynamic system is written as

$$\begin{cases} X(t) = A(t-1)X(t-1) + G(t-1)W(t-1) \\ Z(t) = H(t)X(t) + V(t), \end{cases} \tag{11}$$

where $X(t) = [\,k_d(t)\ c_d(t)\,]^T$ is the state vector; $Z(t) = \Delta F_{\text{act}}(t)$ is the measurement vector; W(t-1) is the measurement noise at $t-1$; V(t) is observation noise; A(t) is the state-transition matrix from $t-1$ to t; G(t) is the system noise matrix; and $H(t) = [\,\Delta p_{act}(t)\ \Delta v_{act}(t)\,]$ is the observation matrix. For the above contact process, the Kalman filter predicts and updates estimation values. The implementation steps of the Kalman filter are given as follows.

Prediction equations:

$$\begin{aligned}\hat{X}(t|t-1) &= A(t-1)\hat{X}(t-1)\\ P(t|t-1) &= A(t-1)P(t-1)A^T(t-1)\\ &\quad + G(t-1)Q(t-1)G^T(t-1).\end{aligned} \tag{12}$$

Update equations:

$$\begin{aligned}K(t) &= P(t|t-1)H^T(t)[H(t)P(t|t-1)H^T(t)+R(t)]^{-1}\\ \hat{X}(t) &= \hat{X}(t|t-1)+K(t)[Z(t)-H(t)\hat{X}(t|t-1)]\\ P(t) &= [I-K(t)H(t)]P(t|t-1)\\ R(t) &= [1-d(t)]R(t-1)+d(t)[y(t)y^T(t)\\ &\quad + H(t)P(t|t-1)H^T(t)],\end{aligned} \tag{13}$$

where $d(t) = (1-b)/(1-b^{t+1})$ is the amnestic factor; and b is the forgetting factor, where $0 < b < 1$. Accordingly, the final state vector contains the estimated stiffness and damping. Thus, the contact parameters can be identified in real time when the increments $\Delta \boldsymbol{F}_{act}(t)$, $\Delta p_{act}(t)$, and $\Delta v_{act}(t)$ are given.

B. DAMPING AMENDMENT

Ideally, the total energy of an undamped satellite system neither increases nor decreases. During the collision and deceleration of flying objects in space, kinetic energy is converted into elastic potential energy. After that, the energy is converted back into kinetic energy, causing the collision rod to rebound. However, as aforementioned, the time delay leads to energy increase. Thus, an energy observer (EO) is designed to monitor the energy flow and an energy controller (EC) is proposed. The EC acts as a variable damping. Once the EO shows that the system is producing energy, the EC activates and the above identified damping is amended in real time.

The EO equations are written as

$$E_{obs}(k) = E(0) + \Delta E_{obs}(k), \tag{14}$$

$$\begin{aligned}\Delta E_{obs}(k) &= \sum_{i=0}^{k}\Big\{[\boldsymbol{F}_{ek}(k)]^T \boldsymbol{v}_{Op}^{des}(k)\boldsymbol{T}_{sam}\\ &\quad + [\boldsymbol{F}_{\alpha}(k-1)]^T \boldsymbol{v}_{Op}^{des}(k-1)\boldsymbol{T}_{sam}\Big\}\\ &\quad + \sum_{i=0}^{k}\Big\{[\boldsymbol{M}_{ek}(k)]^T \boldsymbol{\omega}_{Op}^{des}(k)\boldsymbol{T}_{sam}\\ &\quad + [\boldsymbol{M}_{\alpha}(k-1)]^T \boldsymbol{\omega}_{Op}^{des}(k-1)\boldsymbol{T}_{sam}\Big\},\end{aligned} \tag{15}$$

where $\Delta E_{obs}(k)$ is the energy increment during a contact process; k is the computational time step of discrete integration; T_{sam} is the sampling time; $\boldsymbol{v}_{Op}^{des}(k)$ and $\boldsymbol{\omega}_{Op}^{des}(k)$ are the desired linear and angular velocities at time-step k, respectively; $\boldsymbol{F}_{ek}(k)$ and $\boldsymbol{M}_{ek}(k)$ are elastic contact force and moment at time-step k; and $\boldsymbol{F}_{\alpha}(k-1)$ and $\boldsymbol{M}_{\alpha}(k-1)$ are the EC compensation force and moment at time-step $k-1$.

The contact force can be divided into an elastic force and a damping force. Only the work done by an elastic force can be converted into kinetic energy, whereas the work done by a damping force will be dissipated during a contact process. Thus, the elastic contact force, $\boldsymbol{F}_{ek}(k)$, is written as

$$\boldsymbol{F}_{ek}(k) = \begin{cases}\boldsymbol{F}_{comp}(k-1) - c_d(k-1)\boldsymbol{v}_{Op}^{des}(k-1),\\ \quad \text{if}[\boldsymbol{v}_{Op}^{des}(k)]^T\boldsymbol{F}_{comp}(k) > 0\\ \boldsymbol{F}_{comp}(k) - c_d(k)\boldsymbol{v}_{Op}^{des}(k),\\ \quad \text{if}[\boldsymbol{v}_{Op}^{des}(k)]^T\boldsymbol{F}_{comp}(k) \le 0,\end{cases} \tag{16}$$

where $c_d(k)$ is the above identified damping; $\boldsymbol{F}_{comp}(k)$ is the compensated contact force, defined in next section. Furthermore, for multi-DOF contact in space, since the directions of $\boldsymbol{v}_{Op}^{des}$ and $\boldsymbol{F}_{\text{comp}}$ are not the same, the projection of the desired contact velocity to the contact force is used to calculate the EC compensation force, which is denoted by

$$\boldsymbol{F}_{\alpha}(k) = \frac{\boldsymbol{\alpha}(k)\,\boldsymbol{v}_{Op}^{desT}(k)\,\boldsymbol{F}_{ek}(k)}{\|\boldsymbol{F}_{ek}(k)\|^2}\boldsymbol{F}_{ek}(k), \tag{17}$$

where $\boldsymbol{\alpha}(k)$ is time-varying damping matrix for the amendment. To obtain three components of varying damping, $E_{obs}(k)$ is decomposed into three coordinate axes of the global coordinate system, which is written as

$$E_{obs,i}(k) = E_{obs}(k)\cdot\frac{\|\boldsymbol{F}_{s,i}(k)\|}{\|\boldsymbol{F}_{s}(k)\|}, \quad i = 1,2,3. \tag{18}$$

To guarantee the energy conservation, $E_{obs}(k)$ must be greater than zero for each integration step. Therefore, the amendment damping can be given by

$$\alpha_{i,i}(k) = \begin{cases}-\dfrac{E_{obs,i}(k)}{\frac{\boldsymbol{v}_{des}^T(k)\boldsymbol{F}_{ek}(k)}{\|\boldsymbol{F}_{ek}(k)\|^2}\boldsymbol{F}_{ek,i}(k)\boldsymbol{v}_{des,i}(k)T_{sam}},\\ \quad \text{if } E_{obs,i}(k) < 0\\ 0, \quad \text{if } E_{obs,i}(k) \ge 0\end{cases} \quad i = 1-3, \tag{19}$$

where $\boldsymbol{\alpha}(k) = \boldsymbol{diag}(\alpha_{1,1}(k), \alpha_{2,2}(k), \alpha_{3,3}(k))$.

Substituting Eq. (19) into Eq. (17) yields the EC compensation force, which can eliminate the energy produced by time delay for each computational time-step.

In addition, since the moment measured by the sensor can be calculated by the contact force at the contact point, the EC compensation moment is written as

$$\boldsymbol{M}_{\alpha}(k) = \boldsymbol{r}_{Osp}(k) \times \boldsymbol{F}_{\alpha}(k), \tag{20}$$

where $\boldsymbol{r}_{Osp}(k)$ represents the vector from the origin of the sensor coordinate system to the contact point.

C. COMPENSATION CONTROL SCHEME

This section presents a compensation control strategy, based on the identified parameters. Ideally, the force and moment measured by the six-axis F/T sensor are the inputs of the satellite dynamics. However, as aforementioned, there exist time delays resulted from the measuring system, the dynamic response of the industrial robot. Thus, the measurement force and moment must be compensated to avoid the simulation divergence due to time delay.

Figure 5 shows the compensation process during a HIL simulation. Given the initial displacements, velocities, and

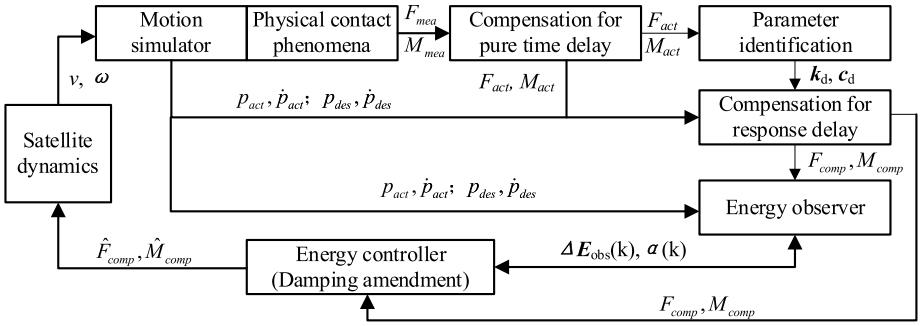

FIGURE 5. Compensation control scheme.

accelerations of two satellites, $\boldsymbol{s}_0$, $\boldsymbol{v}_0$, and $\boldsymbol{a}_0$, respectively, the HIL simulator follows the motion trajectory to realize the first collision between the docking imitation mechanisms. Thus, the six-axis F/T sensor measures the contact force and moment, $\boldsymbol{F}_{\text{mea}}$ and $\boldsymbol{M}_{\text{mea}}$. Moreover, the pure time delay τ_{p} caused by the measurement system is compensated by a low-pass filter, and the actual measuring force and moment $\boldsymbol{F}_{\text{act}}$ and $\boldsymbol{M}_{\text{act}}$ are obtained according to Eq. (6). After that, substituting $\boldsymbol{F}_{\text{act}}$, $\boldsymbol{M}_{\text{act}}$, $\boldsymbol{p}_{\text{Op}}$, and $\boldsymbol{v}_{\text{Op}}$ into Eqs. (8) - (13), the contact stiffness and damping, k_{d} and c_{d}, are identified using the adaptive Kalman filter method.

According to the identified contact stiffness and damping, the compensated contact force for dynamic response delay, $\boldsymbol{F}_{\text{comp}}$, is denoted by

$$\boldsymbol{F}_{err}(t) = k_d \Delta \boldsymbol{p}_{err}(t) + c_d \Delta \boldsymbol{v}_{err}(t), \tag{21}$$

$$\boldsymbol{F}_{comp}(t) = \boldsymbol{F}_{act}(t) + \boldsymbol{F}_{err}(t). \tag{22}$$

where $\Delta \boldsymbol{p}_{err}(t)$ and $\Delta \boldsymbol{v}_{err}(t)$ are the errors of the position and velocity along the direction of measured force, respectively, which are written as

$$\Delta \boldsymbol{p}_{err}(t) = [\boldsymbol{p}_{Op}^{des}(t) - \boldsymbol{p}_{Op}(t)] \cdot \boldsymbol{e}, \tag{23}$$

$$\Delta \boldsymbol{v}_{err}(t) = [\boldsymbol{v}_{Op}^{des}(t) - \boldsymbol{v}_{Op}(t)] \cdot \boldsymbol{e}. \tag{24}$$

where $\boldsymbol{p}_{Op}(t)$ and $\boldsymbol{v}_{Op}(t)$ are the actual position and velocity at the contact point; $\boldsymbol{p}_{Op}^{des}(t)$ and $\boldsymbol{v}_{Op}^{des}(t)$ are the theoretical position and velocity at the contact point, given by

$$\boldsymbol{p}_{Op}^{des}(t) = \boldsymbol{p}_{des}(t) + \boldsymbol{R}_{des}(t)\boldsymbol{r}_{Op}^{Oe}(t), \tag{25}$$

$$\boldsymbol{v}_{Op}^{des}(t) = \boldsymbol{v}_{des}(t) + \omega_{des}(t) \times [\boldsymbol{R}_{des}(t)\boldsymbol{r}_{Op}^{Oe}(t)], \tag{26}$$

where $\boldsymbol{p}_{des}(t)$ is the desired position of the rod center; $\boldsymbol{v}_{des}(t)$ is the desired linear velocity of the contact point; and $\omega_{des}(t)$ is the desired angular velocity of the contact point. These desired values can be calculated using forward kinematic model of the robotic simulator.

Since the point contact does not yield the moment at the contact point, the moment measured by the six-axis F/T sensor is produced by the contact force. Thus, the compensated contact moment, $\boldsymbol{M}_{\text{comp}}$, is given by

$$\begin{aligned}\boldsymbol{M}_{err}(t) = {} & [\boldsymbol{p}_{Op}^{des}(t) - \boldsymbol{p}_{Op}(t)] \times \boldsymbol{F}_{comp}(t) \\ & + [\boldsymbol{p}_{Op}(t) - \boldsymbol{p}_{Os}(t)] \times \boldsymbol{F}_{err}(t),\end{aligned} \tag{27}$$

$$\boldsymbol{M}_{comp}(t) = \boldsymbol{M}_{act}(t) + \boldsymbol{M}_{err}(t), \tag{28}$$

TABLE 1. Simulation parameters.

	Parameter	Unit	Value
Target satellite	Mass	kg	4000
	Initial velocity	mm/s	$v_x = v_y = v_z = 0$
	Moment of inertia	kg·m^2	$I_{xx} = I_{yy} = I_{zz} = 3684$
Servicing satellite	Mass	kg	300
	Initial velocity	mm/s	$v_x = 20$; $v_y = v_z = 0$
	Moment of inertia	kg·m^2	$I_{xx} = I_{yy} = I_{zz} = 98$
Contact parameters	Frequency	Hz	4
	Stiffness	N/mm	176.275
	Damping	N·s/mm	0

Thus, substituting $\boldsymbol{F}_{\text{comp}}$, $\boldsymbol{M}_{\text{comp}}$, $\boldsymbol{v}_{Op}^{des}$, and ω_{Op}^{des} into the EO model yields the revised damping according to Eq. (19), and then the EC compensation force and moment can be obtained using Eqs. (17) and (20). After that, the final estimated contact force and moment, $\hat{\boldsymbol{F}}_{comp}(k)$ and $\hat{\boldsymbol{M}}_{comp}(k)$, can be expressed as

$$\hat{F}_{comp}(k) = \boldsymbol{F}_{comp}(k) + \boldsymbol{F}_{\alpha}(k), \tag{29}$$

$$\hat{M}_{comp}(k) = \boldsymbol{M}_{comp}(k) + \boldsymbol{M}_{\alpha}(k). \tag{30}$$

Finally, $\hat{\boldsymbol{F}}_{comp}$ and $\hat{\boldsymbol{M}}_{comp}$ are substituted into the space dynamic equations, Eqs. (1) and (2), to calculate the new motion trajectory of the robotic simulator, including s, v, and a. Repeating the above steps, the HIL simulation can be continued until the conclusion of the experiment.

IV. SIMULATIONS

In this section, to clarify the effectiveness of parameter identification and damping amendment, three groups of simulations are carried out. The above equations are coded into MATLAB/Simulink software. The virtual model of the simulator is established in the NX/Motion multibody dynamic software. Thus, the co-simulation for the verification can be conducted using both Simulink and NX/Motion. During the co-simulations, contact dynamics is rendered by the NX/Motion software in which contact parameters can be set as fixed values. The stiffness is 176.275 N/mm and the damping is zero. The other parameters for the simulation are shown in Table 1.

A. PARAMETER IDENTIFICATION CONTROL (PIC)

The first group of simulations is to verify the parameter identification, which is called the parameter identification control (PIC). With PIC, the compensated contact forces calculated by Eqs. (22) and (28) are directly substituted into the space contact dynamic equations to produce the motion trajectory of the satellite system and the damping amendment is not involved in the control. The calculation process is presented in an algorithmic form, as seen in Algorithm 1.

Algorithm 1 PIC

Input: $\boldsymbol{v}_s$(k-1) and ω_s(k-1)
Output: $\boldsymbol{v}_s$(k) and ω_s(k)
1: Measure $\boldsymbol{F}_{mea}$ and $\boldsymbol{M}_{mea}$ using the 6-axis F/T sensor
2: Compute $\boldsymbol{F}_{act}$ and $\boldsymbol{M}_{act}$ using Eq. (6)
3: Compute Δp_{act}, Δv_{act}, and ΔF_{act} using Eq. (8) - (9)
4: Estimate k_d and c_d using the adaptive Kalman filter
5: Compute Δp_{err}, Δv_{err}, and F_{err} using Eq. (21), (23), and (24)
6: Compute $\boldsymbol{F}_{comp}$ and $\boldsymbol{M}_{comp}$, using Eq. (22) and (28)
7: Substitute $\boldsymbol{F}_{comp}$ and $\boldsymbol{M}_{comp}$ into Eqs. (1) and (2)
8: Output: $\boldsymbol{v}_s$ and ω_s

Figure 6 (a) and (b) shows the identified results of contact stiffness and damping without the damping amendment. As it can be seen, contact stiffness and damping can be identified by the proposed method. The average errors of contact stiffness for 4 ms and 10 ms delays are 0.23% and 0.43%, respectively. The average errors of contact damping for 4 ms and 10 ms delays are 0.3% and 0.32%, respectively. After three collisions, the identified stiffness almost approaches the desired stiffness. In addition, it is seen that there are negative damping, which results from force measurement noises during discrete contacts. With AKF, the force noise yields large deflection of the estimation error covariance in Eq. (12). Therefore, the negative damping is estimated. In fact, without persistent excitation, the similar results are also generated using other identification methods such as MRAC and RLS [12]. The physical meaning of negative damping can be regarded as the decrease of the system energy. Therefore, substituting a negative damping into the control model compensates the decreased energy.

Figure 6 (c) and (d) gives contact velocities and contact forces. It is found that the contact velocities and forces after compensation are close to the desired velocities and forces. Note that the data between two frames are removed to make the figures larger because there is no contact between the front and rear frames. The errors of contact velocity and force at a 10 ms delay are less than 6% and 10%, respectively. The simulation divergence can be compensated very well by PIC. However, as the time delay increases, the errors between experimental results and the desired data increase. To show the increase more clearly, the results at the second collisions are enlarged in Fig. 6(c) and (d). It can be seen that there are obvious overcompensations of contact force and contact velocity, especially for the 10 ms time delay.

Furthermore, a numerical simulation with a time delay of 20 ms is conducted. Figure 7 shows the desired contact

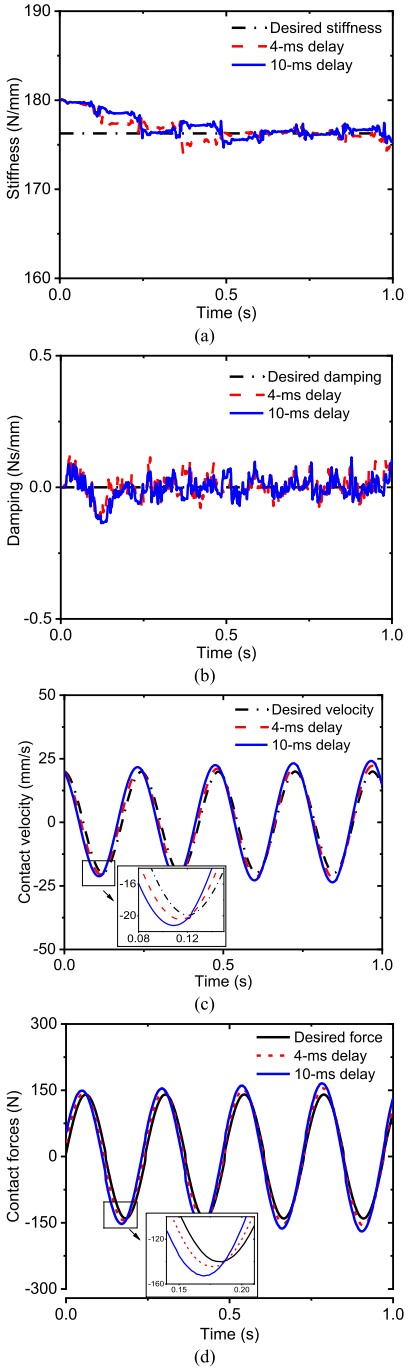

FIGURE 6. Simulation results of the PIC algorithm. (a) contact stiffness. (b) contact damping. (c) contact velocities. (d) contact forces.

velocities and actual velocities after force compensation. Since the stable velocity after each collision is difficult to find because of the absence of the velocities between the front and rear frames (e.g., Fig. 6(c)), the process without contact is also shown in Fig. 7. To show the contact velocities more clearly, a small portion of the figure corresponding to the first contact is enlarged in the inset of Fig. 7. It can be found that the overshoot of contact velocities for the 20 ms time delay increases up to 1.6 times the initial velocity. In the

meantime, the simulation converges quickly for the large time delay. After the first contact, the rebound velocity for the 20 ms time delay is reduced to less than half of the initial velocity. This means the simulation cannot be continued. Accordingly, it can be affirmed that the control without the damping amendment cannot deal with a large time delay.

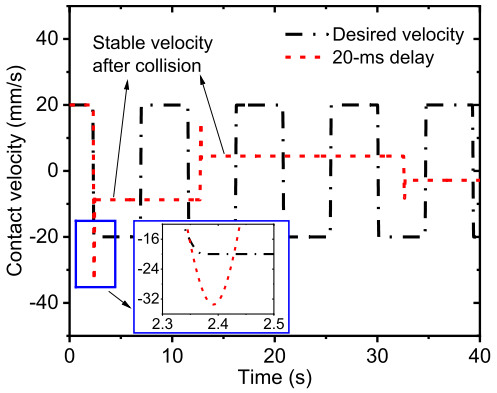

FIGURE 7. Overcompensation due to large time delay.

B. DAMPING AMENDMENT CONTROL (DAC)

In this section, only damping amendment is employed for the control, which is also called the damping amendment control (DAC). With DAC, the measurement delay is compensated, but the dynamic response delay is not compensated. In other words, $\mathbf{F}_{\text{comp}}$ in Eq. (30) is replaced by $\mathbf{F}_{\text{act}}$ in Eq. (13). However, the identified contact damping is still employed for Eq. (30). After that, $\mathbf{F}_{\text{act}}$ is adopted for the calculations of the EO and EC. Finally, the EC compensation force and moment, $\mathbf{F}_{\alpha}$ and $\mathbf{M}_{\alpha}$, are used for solving the motion trajectory of the satellite system. The calculation process is shown in an algorithmic form in Algorithm 2.

Algorithm 2 DAC

Input: $\boldsymbol{v}_{\text{s}}$(k-1) and ω_{s}(k-1)
Output: $\boldsymbol{v}_{\text{s}}$(k) and ω_{s}(k)
1: Measure $\boldsymbol{F}_{\text{mea}}$ and $\boldsymbol{M}_{\text{mea}}$ using the 6-axis F/T sensor
2: Compute $\boldsymbol{F}_{\text{act}}$ and $\boldsymbol{M}_{\text{act}}$ using Eq. (6)
3: Substitute $\boldsymbol{F}_{\text{act}}$(k-1) and $\boldsymbol{M}_{\text{act}}$(k-1) into Eq. (16) yields $\boldsymbol{F}_{\text{ek}}$(k)
4: Substitute $\boldsymbol{F}_{\text{ek}}$(k) and $\boldsymbol{F}_{\alpha}$(k-1) into the EO equations
5: Compute the amendment damping,$\alpha_{\text{i,i}}$(k), using Eq. (19)
6: Compute $\boldsymbol{F}_{\alpha}$(k) and $\boldsymbol{M}_{\alpha}$(k) using Eq.(17) and (20)
7: Replace $\boldsymbol{F}_{\text{comp}}$(k) ($\boldsymbol{M}_{\text{comp}}$(k)) by $\boldsymbol{F}_{\text{act}}$(k) ($\boldsymbol{M}_{\text{act}}$(k)) in Eq. (29) (Eq. (30))
8: Compute $\hat{\boldsymbol{F}}_{comp}\,(k)$ and $\hat{\boldsymbol{M}}_{comp}\,(k)$ using Eq. (29) and (30)
9: Substitute $\hat{\boldsymbol{F}}_{comp}\,(k)$ and $\hat{\boldsymbol{M}}_{comp}\,(k)$ into Eqs. (1) and (2)
10: Output: $\boldsymbol{v}_{\text{s}}$(k) and ω_{s}(k)

To verify the effectiveness of DAC when there is a large time delay, the time delay for the simulation is set as 10 ms. Fig. 8(a) and (b) presents the changes of contact velocity and system energy. The contact velocity does not increase and the simulation system energy remains stable. By applying DAC, the energy increase due to a time delay is resolved. It is also found that there is a phase lead between the desired velocity and the compensated velocity. The reason is that

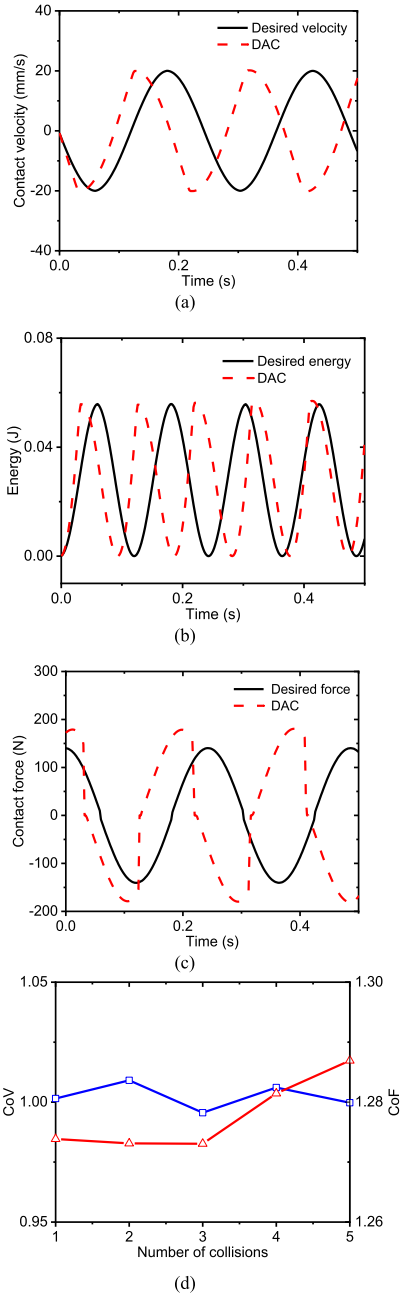

FIGURE 8. Simulation results of the DAC algorithm. (a) contact velocities. (b) energy. (c) contact forces. (d) CoV and CoF.

DAC only compensates the rebounding phase of a contact. Since the time delay leads to energy increase, DAC reduces the increased energy by decreasing the contact time. Thus, the compensated velocities exceed the desired ones. To further evaluate the variation of contact velocity, a coefficient of rebounding velocity (CoV) is defined as the ratio of the rebound velocity to the desired velocity. The CoVs of five collisions are all very close to one, as seen in Fig. 8(d). Therefore, DAC achieves contact velocities closer to the ideal value than PIC for a large time delay. However, there exists an obvious overshoot for the contact force, as seen in Fig. 8(c).

Similarly, a coefficient of contact force (CoF) is defined as the ratio of the maximum contact force to the desired force during one contact cycle. It is found that the CoFs of five collisions are about 1.28. To obtain stable contact velocities, DAC yields large contact forces, which are likely to damage tested instruments.

C. PARAMETER IDENTIFICATION AND DAMPING AMENDMENT (PIDA)

To verify the control with both parameter identification and damping amendment (PIDA), new simulations with the same initial conditions and mass parameters as in Table 1 are conducted. Two time delays (10 ms and 20 ms) are chosen for the simulations. The whole process corresponds to the scheme in Fig. 5. To provide a pseudocode that can be easily executed in real time on the prototype, the calculation process is given in algorithmic form in Algorithm 3.

Algorithm 3 PIDA

Input: $\boldsymbol{v}_{\mathrm{s}}$(k-1) and ω_{s}(k-1)
Output: $\boldsymbol{v}_{\mathrm{s}}$(k) and ω_{s}(k)
1: Measure $\boldsymbol{F}_{\mathrm{mea}}$ and $\boldsymbol{M}_{\mathrm{mea}}$ using the 6-axis F/T sensor
2: Compute $\boldsymbol{F}_{\mathrm{act}}$ and $\boldsymbol{M}_{\mathrm{act}}$ using Eq. (6)
3: Compute Δp_{act}, Δv_{act}, and ΔF_{act} using Eq. (8) - (10)
4: Estimate k_{d} and c_{d} using the adaptive Kalman filter
5: Compute Δp_{err}, Δv_{err}, and F_{err} using Eq. (21), (23), and (24)
6: Compute $\boldsymbol{F}_{\mathrm{comp}}$ and $\boldsymbol{M}_{\mathrm{comp}}$, using Eq. (22) and (28)
7: Substitute $\boldsymbol{F}_{\mathrm{comp}}$(k-1) and $\boldsymbol{M}_{\mathrm{comp}}$(k-1) into Eq. (16) yields $\boldsymbol{F}_{\mathrm{ek}}$(k)
8: Substitute $\boldsymbol{F}_{\mathrm{ek}}$(k) and $\boldsymbol{F}_{\alpha}$(k-1) into the EO equations
9: Compute the amendment damping,$\alpha_{\mathrm{i,i}}$(k), using Eq. (19)
10: Compute $\boldsymbol{F}_{\alpha}$(k) and $\boldsymbol{M}_{\alpha}$(k) using Eq.(17) and (20)
11: Compute $\hat{\boldsymbol{F}}_{comp}\,(k)$ and $\hat{\boldsymbol{M}}_{comp}\,(k)$ using Eq. (29) and (30)
12: Substitute $\hat{\boldsymbol{F}}_{comp}\,(k)$ and $\hat{\boldsymbol{M}}_{comp}\,(k)$ into Eqs. (1) and (2)
13: Output: $\boldsymbol{v}_{\mathrm{s}}$(k) and ω_{s}(k)

Figure 9 shows the contact velocities. For both 10 ms and 20 ms delays, the control with the damping amendment yields stable rebounding velocities that are almost the same as the desired velocities. The CoV is very close to one for each collision. Figure 10 gives the energy comparisons without and with damping amendment. The former leads to quick convergence for the 10 ms time delay but yields significant overcompensations for the 20 ms time delay. In contrast, the latter keeps the system energy stable. In terms of contact forces, DAC yields very large impact forces although it can produce ideal rebound velocities, as seen in Fig. 11. Moreover, the peak value of the contact forces increases with the increase of time delay. Compared to DAC, PIDA yields contact forces very close to the ideal forces for both 10 ms and 20 ms delays. The average CoVs for the 10 ms and 20 ms delays are about 1.05 and 1.16, respectively. Accordingly, PIDA achieves better fidelity in both contact velocity and contact force compared to PIC and DAC.

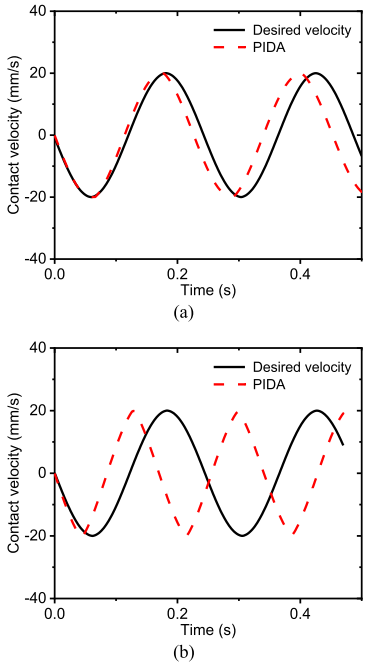

FIGURE 9. Comparisons of contact velocities. (a) 10 ms delay. (b) 20 ms delay.

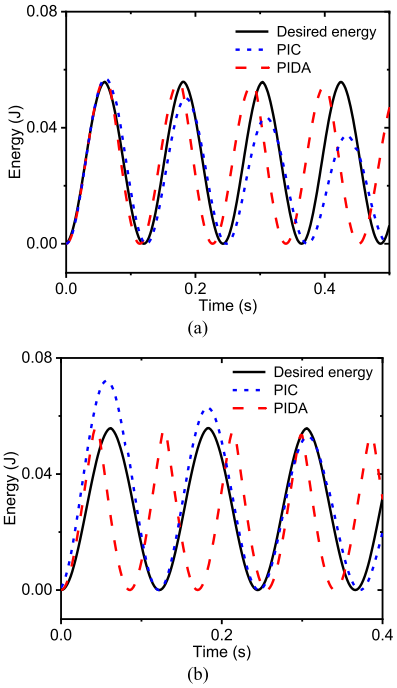

FIGURE 10. Comparisons of energy. (a) 10 ms delay. (b) 20 ms delay.

V. EXPERIMENTS

Figure 12 shows the entire process of a contact experiment as an example. The docking rod first moves along the x-axis with the initial velocity of 20 mm/s and collides with the front frame. The contact velocity decreases to zero, and then the docking rod rebounds toward the rear frame. The rebound velocity is theoretically lower than the initial velocity because of energy dissipation in damped contact. However, simulation divergence due to time delay causes the rebound velocity to be larger than the initial velocity. Experimental results show

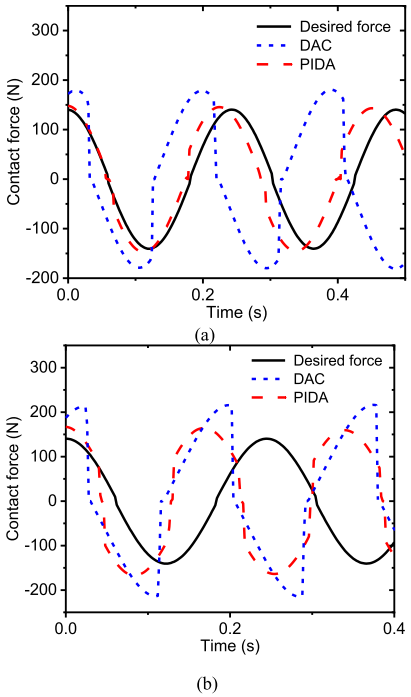

FIGURE 11. Comparisons of contact forces. (a) 10 ms delay. (b) 20 ms delay.

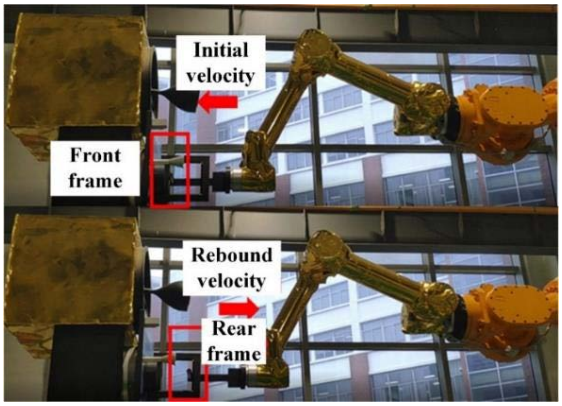

FIGURE 12. Impact experiments.

that the proposed compensation method can eliminate the simulation divergence due to time delay.

A. PARAMETER IDENTIFICATION

Considering contact frequency likely affects parameter identification, collision experiments with different contact frequencies are performed. The contact frequency is determined by both relative mass m_e and contact stiffness k_d, which is written as

$$f = \frac{1}{2\pi}\sqrt{\frac{k_d}{m_e}}, \tag{31}$$

where f is the contact frequency; and the relative mass is equal to $m_s m_t/(m_s + m_t)$, where m_s and m_t are the masses of the service and target satellites, respectively. The relative mass is chosen to represent different experimental cases because contact stiffness changes continually during experiments. For the experiments, two servicing satellite masses are selected as 300 kg and 600 kg. Thus, the corresponding relative masses are 279.07 kg and 521.74 kg. As can be seen in Fig. 13, the average stiffnesses for the two masses, 76.9 N/mm and 77.2 N/mm, are almost the same. Moreover, the average dampings for two masses are all approximately 0.13 N·s/mm. According to the estimated average stiffness, the contact frequencies are 2.64 Hz and 1.93 Hz. Accordingly, the consistency of the identified results in regard to different frequencies validates the proposed parameter identification algorithm.

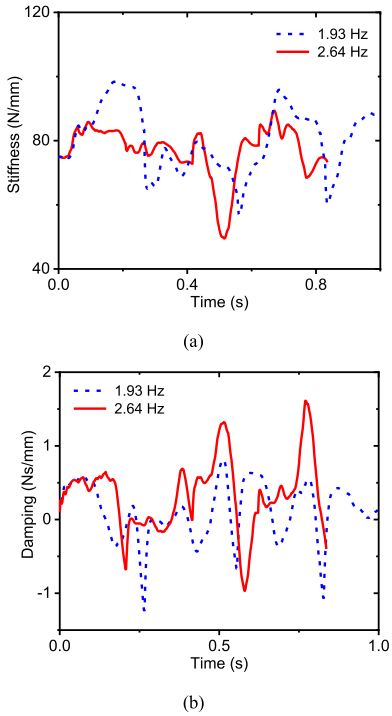

FIGURE 13. Experimental results for parameter identification. (a) contact stiffness. (b) contact damping.

B. CONTACT VELOCITY AND ENERGY

Figure 14 gives the contact velocities for different contact frequencies. There exists obvious velocity divergence without control, which renders the experiment unable to be continued. It is found that velocity divergence due to time delay can be decreased by applying PIC, DAC, and PIDA. PIC leads to an overshoot of contact velocity, whereas DAC and PIDA do not. With the increase of contact frequency, the rebound velocity converges quickly. As can be seen in Fig. 14(b), the rebound velocity decreases by up to half of the initial velocity after four collisions, even with PIDA. With PIC, the rebound velocity reaches approximately zero after four collisions. This shows PIDA compensates contact velocity much better than PIC.

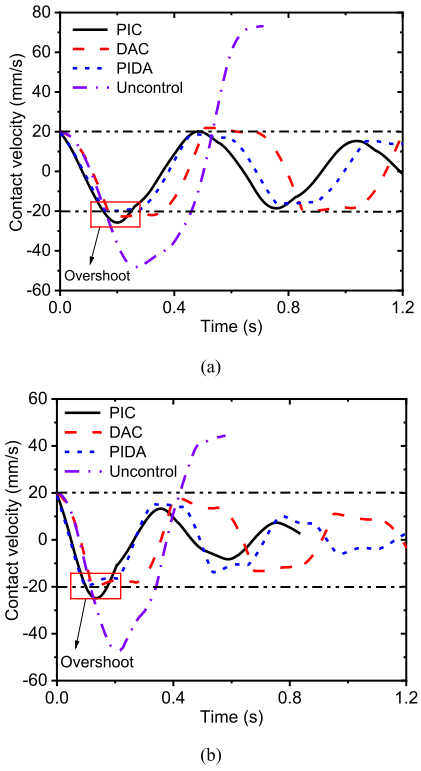

FIGURE 14. Contact velocities in experiments. (a) f = 1.93Hz. (b) f = 2.64 Hz.

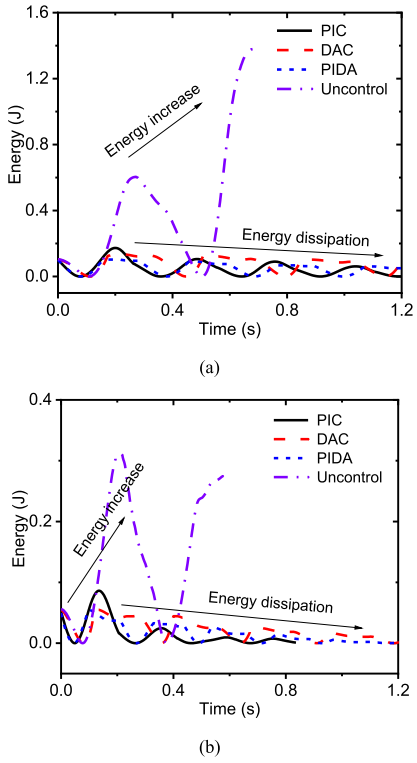

FIGURE 15. Energy dissipation in experiments. (a) f = 1.93Hz. (b) f = 2.64 Hz.

Furthermore, as seen in Fig.15, the kinetic energy increases sharply when there is no control, whereas the kinetic energy dissipates when PIC, DAC, and PIDA are used. In the present study, the damping force is considered in the proposed DAC and PIDA by substituting the identified damping into the EC. Although a theoretical control with the energy conservation produces constant rebounding velocity, the damping of the simulation system is bound to yield velocity convergence and energy dissipation. Thus, the energy dissipation more closely reflects the reality. In the meantime, it is also found that PIC generates quick convergence because of large time delay of the simulator. With the increase of contact frequency, the dissipation speed of kinetic energy also increases. However, DAC and PIDA can maintain the simulation with normal speed of the practical energy dissipation.

C. CONTACT FORCE

Figure 16 gives the measured forces and compensated forces when the contact frequency is 1.93 Hz. As can be seen in Fig. 16(a), there is an obvious time delay between measured forces and compensated forces. The phase of compensated force is kept close to the desired position. Therefore, velocity divergence is prohibited. DAC does not adjust measured forces during the deceleration process, but it sharply decreases the contact force to meet the requirement of energy conservation during the rebounding process. Moreover, DAC generates large contact forces to reduce velocity divergence,

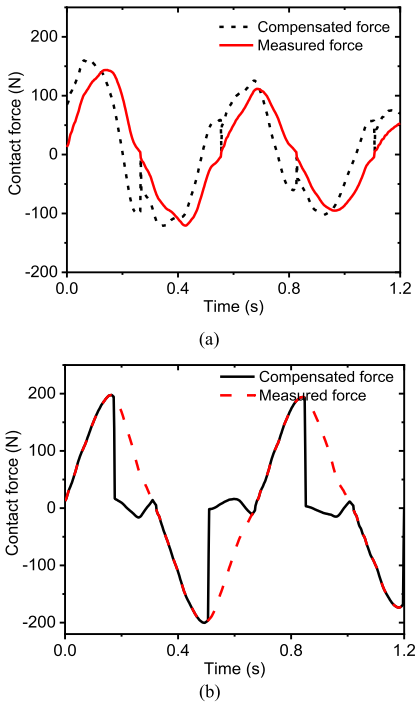

FIGURE 16. Comparison of measured and compensated forces (f = 1.93 Hz). (a) The PIC method. (b) The DAC method.

as seen in Fig. 17. The measured contact forces with DAC are much larger than those with PIC and PIDA. In other words, DAC sacrifices the fidelity of contact forces to achieve

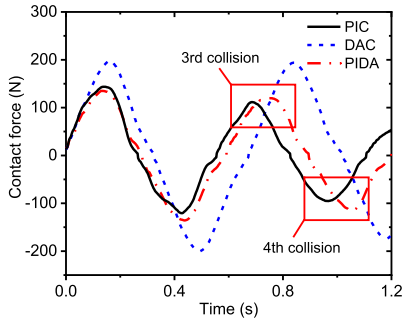

(a)

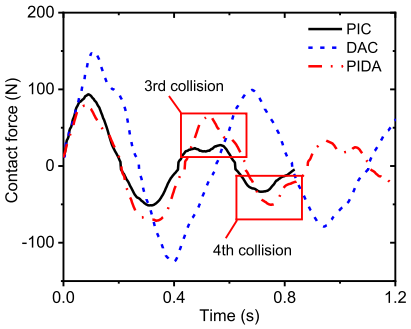

(b)

FIGURE 17. Measured forces in experiments. (a) f = 1.93 Hz. (b) f = 2.64 Hz.

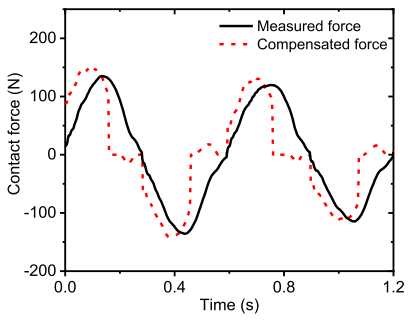

(a)

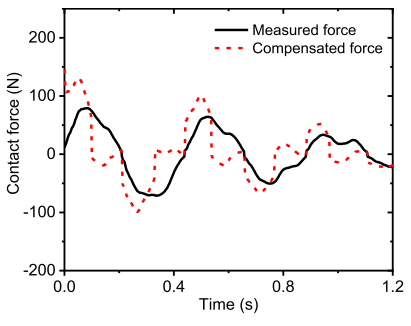

(b)

FIGURE 18. Comparison of measured and compensated forces for PIDA method. (a) f = 1.93 Hz. (b) f = 2.64 Hz.

stable contact velocities. Furthermore, the measured force is the practical contact force between the docking imitation mechanisms. The large contact force is very likely to damage tested instruments. However, PIDA directly compensates the time delay of contact force, as seen in Fig. 18. The compensated force of PIDA has an obvious phase lead compared to the measured force. Moreover, PIDA produces appropriate contact forces. Compared with PIC, PIDA can still generate larger practical contact forces at the third and fourth collisions, as depicted in Fig. 17. Thus, PIDA is capable of maintaining simulation experiments, whereas PIC leads to quick velocity convergence (Fig. 14), especially for higher contact frequency. Accordingly, PIDA obtains the fidelity of both contact velocity and contact force during the HIL simulation experiments.

VI. CONCLUSION

In this study, a measurement compensation method is proposed to ensure a faithful and reliable HIL simulation of space robotic operation. A real-time estimation method for contact stiffness and damping is proposed based on the adaptive Kalman filter. After that, a EO is designed to monitor the energy flow and thus a EO model is derived to calculate the damping amendment. Furthermore, based on the parameter identification and damping amendment, three control algorithms are proposed. To clarify clearly the effectiveness of the proposed method (PIDA), the other two compensation algorithms, namely PIC and DAC, are presented and compared with the PIDA. All three methods are based on the proposed parameter identification algorithm. It is found that the contact parameters can be identified very well for different time delays. The average errors of contact stiffness and damping at a 10 ms delay are only 0.43% and 0.32%, respectively. The PIC algorithm can prevent simulation divergence for time delays of 10 ms or smaller. Compared to PIC, the DAC algorithm can reproduce much more steady contact velocities while DAC yields large contact forces. Only through the PIDA algorithm, high fidelities of both contact force and contact velocity can be achieved in the HIL simulation.

REFERENCES

[1] G. Li and P. Xu, "Design and analysis of a deployable grasping mechanism for capturing non-cooperative space targets," *Aerosp. Sci. Technol.*, vol. 106, Nov. 2020, Art. no. 106230.
[2] X. Wang, L. Shi, and J. Katupitiya, "A strategy to decelerate and capture a spinning object by a dual-arm space robot," *Aerosp. Sci. Technol.*, vol. 113, Jun. 2021, Art. no. 106682.
[3] Z. Wei, H. Wen, H. Hu, and D. Jin, "Ground experiment on rendezvous and docking with a spinning target using multistage control strategy," *Aerosp. Sci. Technol.*, vol. 104, Sep. 2020, Art. no. 105967.
[4] A. Flores-Abad, O. Ma, K. Pham, and S. Ulrich, "A review of space robotics technologies for on-orbit servicing," *Prog. Aerosp. Sci.*, vol. 68, pp. 1–26, Jul. 2014.
[5] O. Ma, J. Wang, S. Misra, and M. Liu, "On the validation of SPDM task verification facility," *J. Field Robot.*, vol. 21, no. 5, pp. 219–235, 2004.
[6] K. Osaki, A. Konno, and M. Uchiyama, "Delay time compensation for a hybrid simulator," *Adv. Robot.*, vol. 24, nos. 8–9, pp. 1081–1098, Jan. 2010.
[7] F. Gao, C. Qi, A. Ren, X. Zhao, R. Cao, Q. Sun, Q. Wang, Y. Hu, J. He, Z. Jin, R. Liu, Y. Zhang, W. Guo, Z. Hu, P. Tang, B. Ni, Q. Jing, W. Wang, and P. Gao, "Hardware-in-the-loop simulation for the contact dynamic process of flying objects in space," *Sci. China Technolog. Sci.*, vol. 59, no. 8, pp. 1167–1175, Jul. 2016.
[8] C. Qi, F. Gao, X. Zhao, A. Ren, and Q. Wang, "A force compensation approach toward divergence of Hardware-in-the-Loop contact simulation system for damped elastic contact," *IEEE Trans. Ind. Electron.*, vol. 64, no. 4, pp. 2933–2943, Apr. 2017.

[9] Y. She, S. Li, and J. Hu, "Contact dynamics and relative motion estimation of non-cooperative target with unilateral contact constraint," *Aerosp. Sci. Technol.*, vol. 98, Mar. 2020, Art. no. 105705.
[10] S. Yu, J. Han, Z. Qu, and Y. Yang, "A force and displacement compensation method toward divergence and accuracy of hardware-in-the-loop simulation system for manipulator docking," *IEEE Access*, vol. 6, pp. 35091–35104, 2018.
[11] S. Yu, J. Han, Y. Yang, D. Xu, and Z. Qu, "Force and moment compensation method based on three degree-of-freedom stiffness-damping identification for manipulator docking hardware-in-the-loop simulation system," *IEEE Access*, vol. 6, pp. 63452–63467, 2018.
[12] D. Erickson, M. Weber, and I. Sharf, "Contact stiffness and damping estimation for robotic systems," *Int. J. Robot. Res.*, vol. 22, no. 1, pp. 41–57, Jan. 2003.
[13] H. Seraji and R. Colbaugh, "Force tracking in impedance control," *Int. J. Robot. Res.*, vol. 16, no. 1, pp. 97–117, Feb. 1997.
[14] S. K. Singh and D. O. Popa, "An analysis of some fundamental problems in adaptive control of force and impedance behavior: Theory and experiments," *IEEE Trans. Robot. Autom.*, vol. 11, no. 6, pp. 912–921, Dec. 1995.
[15] L. J. Love and W. J. Book, "Environment estimation for enhanced impedance control," in *Proc. IEEE Int. Conf. Robot. Autom.*, May 1995, pp. 1854–1859.
[16] X. Gao, D. You, and S. Katayama, "Seam tracking monitoring based on adaptive Kalman filter embedded Elman neural network during high-power fiber laser welding," *IEEE Trans. Ind. Electron.*, vol. 59, no. 11, pp. 4315–4325, Nov. 2012.
[17] O. Ma, A. Flores-Abad, and T. Boge, "Use of industrial robots for hardware-in-the-loop simulation of satellite rendezvous and docking," *Acta Astronautica*, vol. 81, no. 1, pp. 335–347, Dec. 2012.
[18] M. D. Stefano, R. Balachandran, and C. Secchi, "A passivity-based approach for simulating satellite dynamics with robots: Discrete-time integration and time-delay compensation," *IEEE Trans. Robot.*, vol. 36, no. 1, pp. 189–203, Feb. 2020.
[19] C. Secchi, S. Stramigioli, and C. Fantuzzi, *Control of Interactive Robotic Interfaces: A Port-Hamiltonian Approach* (Springer Tracts in Advanced Robotics). Berlin, Germany: Springer, 2007.
[20] N. Diolaiti, G. Niemeyer, F. Barbagli, and J. K. Salisbury, "Stability of haptic rendering: Discretization, quantization, time delay, and Coulomb effects," *IEEE Trans. Robot.*, vol. 22, no. 2, pp. 256–268, Apr. 2006.
[21] P. F. Hokayem and M. W. Spong, "Bilateral teleoperation: An historical survey," *Automatica*, vol. 42, no. 12, pp. 2035–2057, Dec. 2006.
[22] B. Hannaford and J. H. Ryu, "Time domain passivity control of haptic interfaces," in *Proc. IEEE Int. Conf. Rob. Auto. (ICRA)*, Seoul, South Korea, May 2001, pp. 1863–1869.
[23] J.-H. Ryu, C. Preusche, B. Hannaford, and G. Hirzinger, "Time domain passivity control with reference energy following," *IEEE Trans. Control Syst. Technol.*, vol. 13, no. 5, pp. 737–742, Sep. 2005.
[24] M. D. Stefano, J. Artigas, W. Rackl, and A. Albu-Schaeffer, "Passivity of virtual free-floating dynamics rendered on robotic facilities," in *Proc. IEEE Int. Conf. Rob. Auto. (ICRA)*, May 2015, pp. 781–788.
[25] M. De Stefano, R. Balachandran, J. Artigas, and C. Secchi, "Reproducing physical dynamics with hardware-in-the-loop simulators: A passive and explicit discrete integrator," in *Proc. IEEE Int. Conf. Robot. Autom. (ICRA)*, May 2017, pp. 5899–5906.

JUN HE received the Ph.D. degree in mechanical engineering from the School of Mechanical Engineering, Shanghai Jiao Tong University.

He is currently an Associate Professor with the School of Mechanical Engineering, Shanghai Jiao Tong University. As a Project Leader, he was engaged in the National Natural Science Foundation of China. His research interest includes mechanism and robotics in space.

MINGJIN SHEN received the B.S. degree in mechanical engineering from Ningbo University and the M.S. degree in mechanical engineering from the School of Mechanical Engineering, Shanghai Jiao Tong University.

As a Key Member, he was involved in the National Natural Science Foundation of China. His research interest includes design and control of space robots.